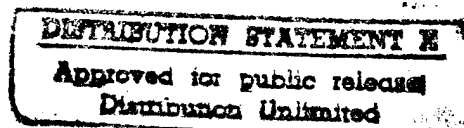


Quarterly Technical Report

Growth, Characterization and Device Development in Monocrystalline Diamond Films

Supported under Grant #N00014-93-I-0437
Office of the Chief of Naval Research
Report for the period 1/1/96-3/31/96



R. F. Davis, R. J. Nemanich* and Z. Sitar
S. P. Bozeman, M. T. McClure, and C. Wolden
North Carolina State University
c/o Materials Science and Engineering Department
Box 7907

*Department of Physics
Raleigh, NC 27695

19960509 137

March, 1996

REPORT DOCUMENTATION PAGE			Form Approved OMB No. 0704-0188	
Public reporting burden for this collection of information is estimated to average 1 hour per response, including the time for reviewing instructions, searching existing data sources, gathering and maintaining the data needed, and completing and reviewing the collection of information. Send comments regarding this burden estimate or any other aspect of this collection of information, including suggestions for reducing this burden to Washington Headquarters Services, Directorate for Information Operations and Reports, 1215 Jefferson Davis Highway, Suite 1204, Arlington, VA 22202-4302, and to the Office of Management and Budget Paperwork Reduction Project (0704-0188), Washington, DC 20503.				
1. AGENCY USE ONLY (Leave blank)		2. REPORT DATE March, 1996		3. REPORT TYPE AND DATES COVERED Quarterly Technical 1/1/96-3/31/96
4. TITLE AND SUBTITLE Growth, Characterization and Device Development in Monocrystalline Diamond Films			5. FUNDING NUMBERS s400003srr14 1114SS N00179 N66005 4B855	
6. AUTHOR(S) R. F. Davis, R. J. Nemanich, and Z. Sitar				
7. PERFORMING ORGANIZATION NAME(S) AND ADDRESS(ES) North Carolina State University Hillsborough Street Raleigh, NC 27695			8. PERFORMING ORGANIZATION REPORT NUMBER N00014-93-I-0437	
9. SPONSORING/MONITORING AGENCY NAME(S) AND ADDRESS(ES) Sponsoring: ONR, Code 312, 800 N. Quincy, Arlington, VA 22217-5660 Monitoring: Admin. Contracting Officer, ONR, Regional Office Atlanta 101 Marietta Tower, Suite 2805 101 Marietta Street Atlanta, GA 30323-0008			10. SPONSORING/MONITORING AGENCY REPORT NUMBER	
11. SUPPLEMENTARY NOTES				
12a. DISTRIBUTION/AVAILABILITY STATEMENT Approved for Public Release; Distribution Unlimited			12b. DISTRIBUTION CODE	
13. ABSTRACT (Maximum 200 words) A combination of <i>in-situ</i> microprobe sampling and detailed chemical kinetic modeling has been employed to provide insight into the mechanisms of nucleation and growth of high quality diamond films in combustion flame CVD. Growth of high quality diamond with large area uniformity has been accomplished. The effects of substrate temperature and gas ratio on morphology and quality are reported. <i>In-situ</i> measurements of gas phase species are described. Calculations were performed using the CHEMKIN package. Equilibrium and premixed laminar flame simulations were performed. Diamond deposition was also performed on TiC(111) substrates by microwave plasma CVD. The diamond (111) pole figure showed a (111) fiber texture in the deposited layer. Approximately 16% of the diamond particles were oriented with the substrate. Nuclear transmutation of B to Li is being investigated for donor doping of diamond. Homoepitaxial ¹⁰ B enriched diamond films have been grown and characterized prior to irradiation using Hall measurements and Raman and photoluminescence spectroscopy. The films have been neutron-irradiated at a dose of 3x10 ²⁰ n/cm ² . The samples showed an activity of approximately 3 mCi of ⁴⁶ Sc when removed from the reactor, probably because of impurities in the natural diamond substrates.				
14. SUBJECT TERMS diamond, microprobe sampling, chemical kinetic modeling, nucleation, growth, CVD, combustion flame, gas phase species, laminar flame, microwave plasma, TiC, fiber texture, nuclear transmutation, donor doping, neutron irradiation			15. NUMBER OF PAGES 31	
			16. PRICE CODE	
17. SECURITY CLASSIFICATION OF REPORT UNCLAS	18. SECURITY CLASSIFICATION OF THIS PAGE UNCLAS	19. SECURITY CLASSIFICATION OF ABSTRACT UNCLAS	20. LIMITATION OF ABSTRACT SAR	

Table of Contents

I.	Introduction	1
II.	An Investigation of Low Pressure Combustion Chemical Vapor Deposition of Diamond <i>C. Wolden and Z. Sitar</i>	2
III.	Texture Analysis of Diamond Particles Deposited on TiC(111) by MPCVD <i>M. McClure and Z. Sitar</i>	20
IV.	Donor Doping of Diamond using Nuclear Transmutation <i>S. P. Bozeman, R. J. Nemanich and R. F. Davis</i>	27
V.	Distribution List	31

I. Introduction

Diamond as a semiconductor in high-frequency, high-power transistors has unique advantages and disadvantages. Two advantages of diamond over other semiconductors used for these devices are its high thermal conductivity and high electric-field breakdown. The high thermal conductivity allows for higher power dissipation over similar devices made in Si or GaAs, and the higher electric field breakdown makes possible the production of substantially higher power, higher frequency devices than can be made with other commonly-used semiconductors.

In general, the use of bulk crystals severely limits the potential semiconductor applications of diamond. Among several problems typical for this approach are the difficulty of doping the bulk crystals, device integration problems, high cost and low area of such substrates. In principal, these problems can be alleviated via the availability of chemically vapor deposited (CVD) diamond films. Recent studies have shown that CVD diamond films have thermally activated conductivity with activation energies similar to crystalline diamonds with comparable doping levels. Acceptor doping via the gas phase is also possible during activated CVD growth by the addition of diborane to the primary gas stream.

The recently developed activated CVD methods have made feasible the growth of polycrystalline diamond thin films on many non-diamond substrates and the growth of single crystal thin films on diamond substrates. More specifically, single crystal epitaxial films have been grown on the {100} faces of natural and high pressure/high temperature synthetic crystals. Crystallographic perfection of these homoepitaxial films is comparable to that of natural diamond crystals. However, routes to the achievement of rapid nucleation on foreign substrates and heteroepitaxy on one or more of these substrates has proven more difficult to achieve. This area of study has been a principal focus of the research of this contract.

At present, the feasibility of diamond electronics has been demonstrated with several simple experimental devices, while the development of a true diamond-based semiconductor materials technology has several barriers which a host of investigators are struggling to surmount. It is in this latter regime of investigation that the research described in this report has and continues to address.

In this reporting period, (1) *in situ* microprobe sampling and detailed chemical kinetic modeling has been employed to provide insight into the mechanisms of nucleation and growth of high-quality diamond films in combustion flame CVD, (2) diamond deposition was achieved on TiC(111) substrates by microwave plasma CVD with approximately 16% of the particles oriented with the substrate, and (3) efforts regarding the nuclear transmutation of ^{10}B to Li were initiated for donor doping of diamond. The following sections are self-contained in that they present an introduction, the experimental procedures, results and discussion, summary and indications of future research for the given research thrust.

II. An Investigation of Low Pressure Combustion Chemical Vapor Deposition of Diamond

A. Introduction

Pioneered by Hirose [0], combustion CVD employed conventional oxyacetylene welding torches to achieve diamond synthesis at extremely fast growth rates, but these films suffer from radial non-uniformity. The use of laminar flat flames at both atmospheric [1,2] and reduced pressures [3,4] has been used to achieve large area uniformity. Although it has been suggested that flame synthesis is the most flexible diamond CVD process [5], commercialization has been limited by high operating costs (primarily the expense of acetylene). Thus, growth rates need to be improved while maintaining high quality.

Another reason for studying the stagnation flow flame is that it is amenable to detailed kinetic modeling. The combustion flame may be the best suited diamond CVD system for kinetic modeling. The chemistry of acetylene flames is well understood due to extensive work in the combustion field [6,7]. In contrast, hot-filament and plasma systems are dominated by heterogeneous chemistry [8] and plasma kinetics [9], neither of which is well understood. By combining modeling with *in-situ* species measurements we hope to shed light on the growth mechanism. After developing an understanding of the oxy-acetylene flame, the kinetic code may be used to quickly assess the performance of additives and alternative fuels.

B. Procedure

Experimental Approach. The experimental system is schematically shown in Fig. 1. The burner is housed in a water-cooled chamber that has been used in previous combustion studies at N. C. State [10]. The present system has been modified by the construction of a new burner and a new substrate stage. The burner is a Powling-type design [11] which is housed in a water-cooled 0.5" O.D. stainless steel tube. Typically substrates are 2" (100) silicon wafers that are clamped on the 3" diameter water-cooled copper stage. The substrates are pre-scratched in an ultrasonic bath of acetone and submicron diamond particles to ensure a high nucleation density. A high voltage feedthrough is used to ignite the flame. Substrate temperature was monitored and controlled using a single color pyrometer. Feedback control maintained the desired substrate temperature within ± 3 °C during deposition, but the absolute temperature may be off by as much as 50 °C due to the limitations of the single color pyrometer.

The copper cooling stage has a 0.25" hole in the center to permit the introduction of a quartz microprobe to sample gases that impinge upon the substrate as shown in Fig. 1. Species entering the quartz probe are transported to the sampling system shown in Fig. 2, and detected by a quadrupole mass spectrometer (QMS). The reduced pressure in the quartz probe (~0.2 Torr) and the associated cooling due to expansion combine to effectively quench the sampled gases at the composition that entered the probe [12].

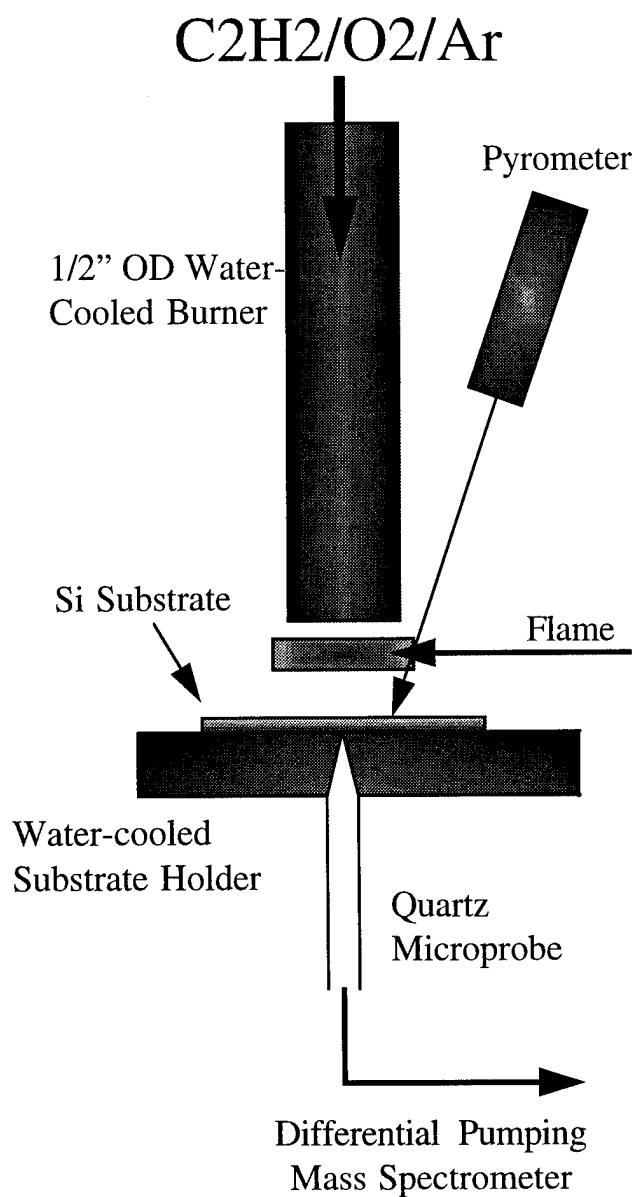


Figure 1. Schematic drawing of the flat flame deposition system.

Although there are at least 50 species that contribute to the chemistry of these flames, the following six molecules are expected to account for > 99% of all stable species: CO, H₂, H₂O, CO₂, C₂H₂, and CH₄ [7,8]. As shown in Table I, these species may be measured without requiring extensive deconvolution of the spectrum. In all experiments, argon is used as a diluent to compensate for mass discrimination effects. One may relate signals measured by the mass spectrometer to mole fractions in the combustion chamber using the expression [13]:

$$\frac{I_i}{I_{Ar}} = S_{i,Ar} \frac{X_i}{X_{Ar}} \quad (1)$$

where I_i is the measured intensity of species i , and X_i is its mole fraction. The sensitivity factor, $S_{i,Ar}$, accounts for mass discrimination effects that arise due to differences in ionization cross-sections or gas dynamics during sampling. $S_{i,Ar}$ is measured in independent experiments using calibrated mixtures of argon and stable gases. In addition, by always measuring signals relative to Ar, problems associated with fluctuations in the ionizer or detector are minimized.

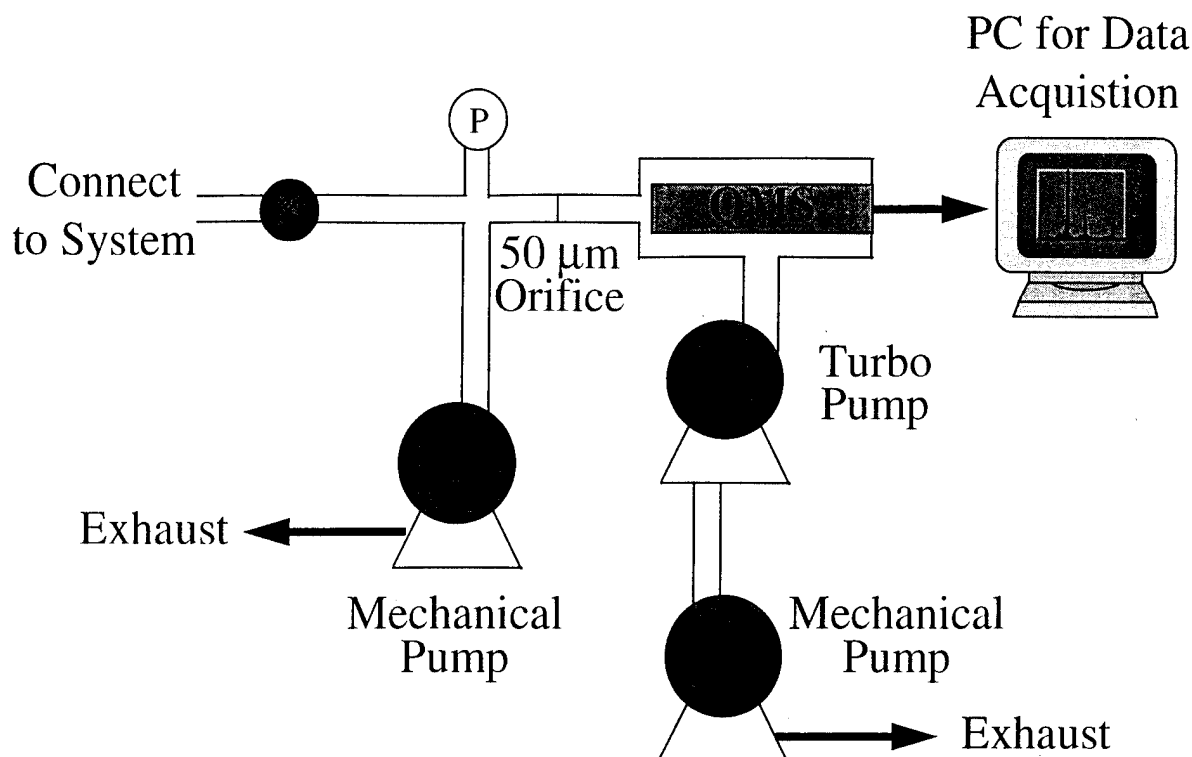


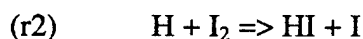
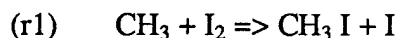
Figure 2. Gas-sampling and detection system.

Table I. Major Stable Flame Species and the Channels (m/e) Where They Will Be Monitored.

Species	m/e Channels						
	2	15	18	26	28	40	44
H ₂	X(100)						
CH ₄		X(86)					
H ₂ O			X(100)				
C ₂ H ₂				X(100)			
CO					X(100)		
Ar						X(100)	
CO ₂					X(8)		X(100)

The number in the parenthesis indicates the percentage relative to the major peak for that species.

Currently we have the capability to sample stable species. By introducing iodine vapor into the sampling probe we plan to detect methyl radical and atomic hydrogen through scavenging techniques [14]. The radicals rapidly react with iodine as shown:



Free iodine atoms simply recombine and the stable species are detected.

Modeling Approach. The modeling formalism employs the CHEMKIN II collection of software [15]. CHEMKIN II consists of FORTRAN subroutines which evaluate the kinetics, equilibrium constants, and transport properties of gas-phase species. Capabilities include surface kinetics, although these kinetics are typically not well known. Different subroutines solve detailed kinetics in zero and one-dimensional idealized flow systems. The pertinent system for combustion CVD of diamond is the rotating disk/stagnation flow CVD code named SPIN [16]. The schematic of the flow geometry is shown schematically in Fig. 3. A uniform axial flow with specified temperature and composition enters the reactor at $z=0$, and approaches a rotating susceptor located at a distance $z = L$ away. Under proper operating conditions, the complex 3-dimensional flow problem may be reduced to a solution dependent only on the axial coordinate through the use of a similarity transformation [17]. In our case, the rotation rate is $\Omega = 0$, however, the solution is still valid as the forced convection nature of the flame results in the identical stagnation flow condition. This procedure has been previously used to model diamond deposition for both atmospheric flames [18] and DC arc-jets [19]. In contrast to these previous results, we will compare simulations directly with measured species profiles.

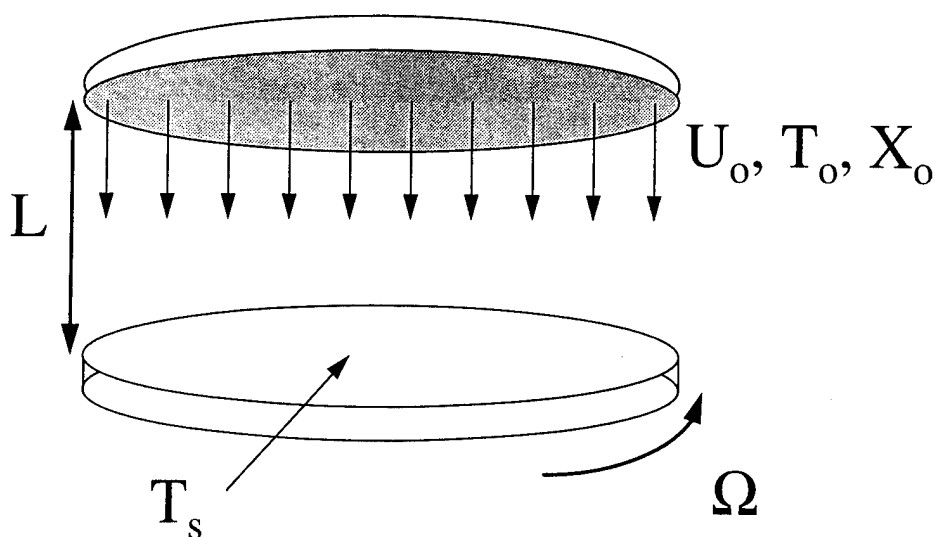


Figure 3. Rotating disk/stagnation flow CVD geometry.

C. Results

Deposition. High-quality deposition has been achieved at significant growth rates, and over large areas. Figure 4 shows the radial dependence of morphology of a typical film deposited in our system as observed by scanning electron microscopy (SEM). The deposition conditions were as follows: $T_s = 850^\circ\text{C}$, $P = 40$ Torr, $z =$ burner-substrate distance $= 13$ mm, $R = \text{O}_2:\text{C}_2\text{H}_2 = 1.00$ ($\phi = 2.50$). The deposition time was 62 minutes. Well-faceted diamond is deposited over an area of diameter greater than 26 mm. The film is completely uniform over the diameter of the burner (11 mm), while a decrease in grain size is observed at the radius increases. Raman spectroscopy results shown in Fig. 5 are consistent with the SEM micrographs. Throughout the radial profile, the sharp diamond peak at 1332 cm^{-1} is found; however, the background luminescence increases with radial position. This is attributed to scattering which is inversely proportional to the grain size. Cross-section SEMs of the

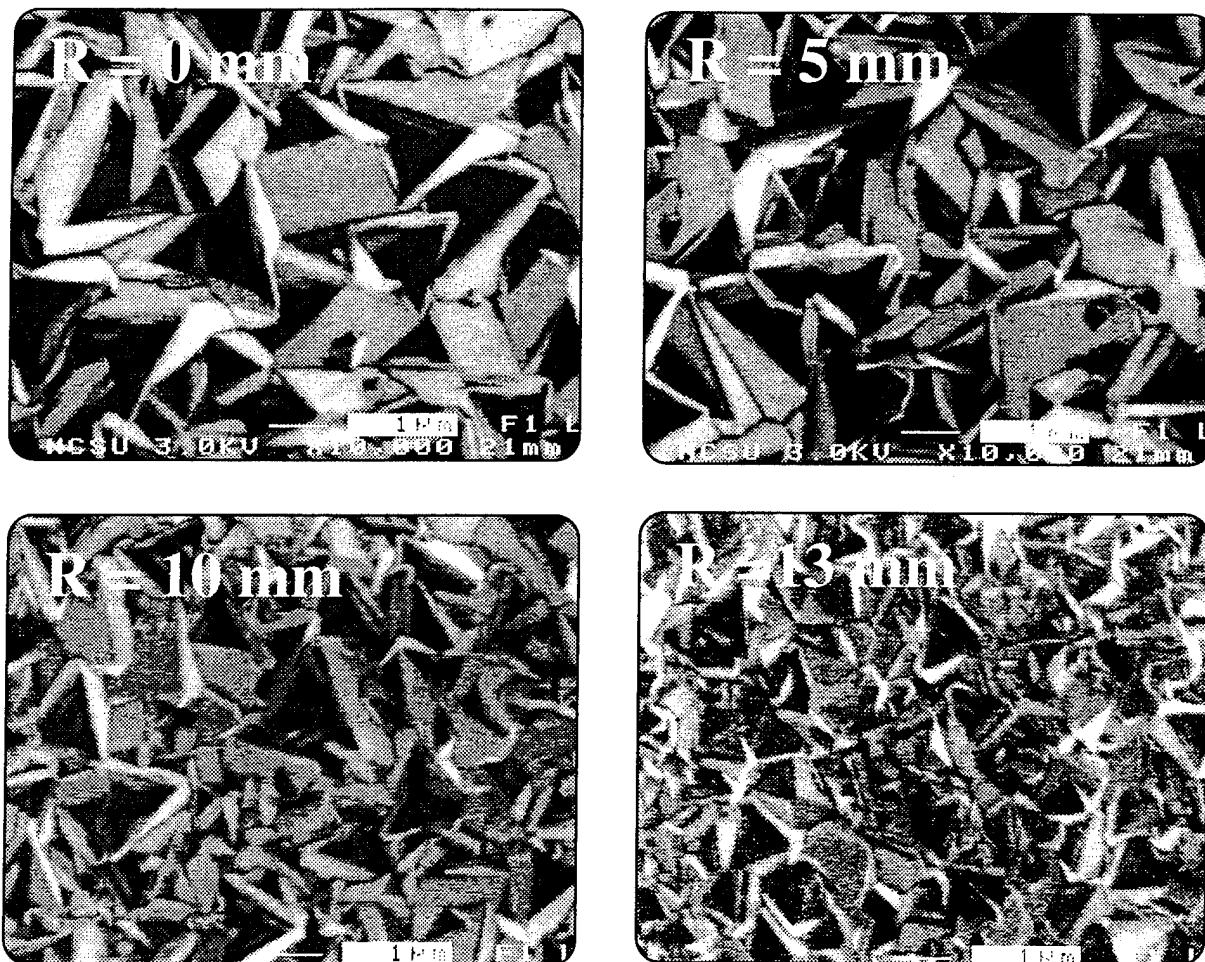


Figure 4. Radial morphology variation. Growth conditions: $T = 850^\circ\text{C}$, $P = 40$ Torr, $R = 1.00$.

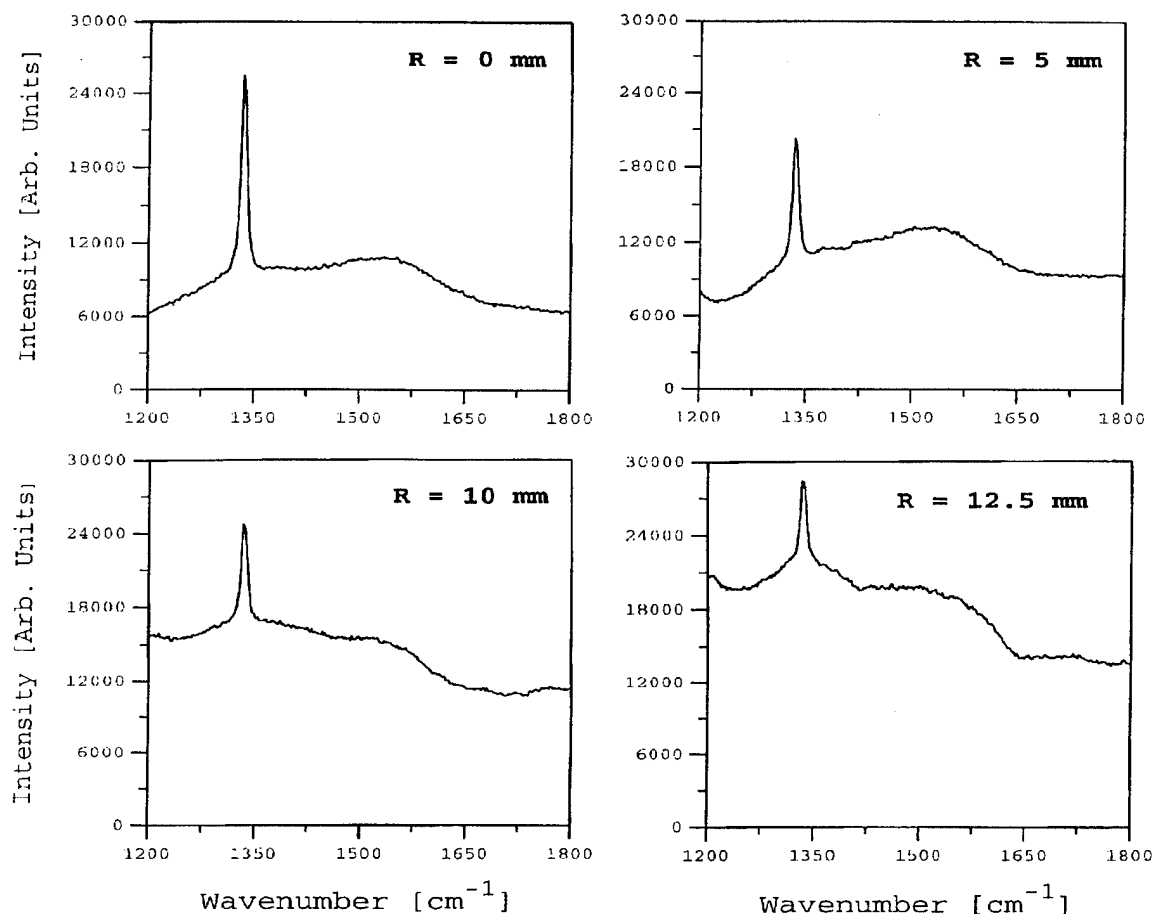


Figure 5. Radial variation in Raman spectrum. Positions correspond to SEM images in Fig. 4.

deposited films indicate a growth rate of $\sim 5 \mu\text{m/hr}$. These are the highest growth rates reported for a low pressure combustion process. It is expected that further increases in the growth rate may be achieved by excluding the 5% argon diluent that is currently used to calibrate the mass spectrometer.

In addition, the dependence of film quality on substrate temperature and gas composition have been assessed. Figures 6 and 7 show the impact of substrate temperature between 700 and 900 °C as observed by SEM and Raman spectroscopy. Below 850 °C there is not a strong effect on either morphology or crystallinity, although quality decreases sharply as the temperature is further increased. In all our samples, the observed preferential orientation is $\langle 111 \rangle$, as indicated by the characteristic triangular facets seen in Figs. 4 and 6. We are currently attempting to find conditions which promote $\langle 100 \rangle$ textured growth.

A very sharp dependence on gas-phase composition is observed. All the high quality diamond has been deposited at $R = 1.000$. A small decrease in the amount of oxygen ($R = 0.975$) results in nothing but graphitic or diamond-like carbon deposition as detailed in Figs. 8 and 9. An increase of oxygen to $R = 1.025$ results in etching or no growth. The strong dependence on composition is unaffected over the temperature range examined to date.

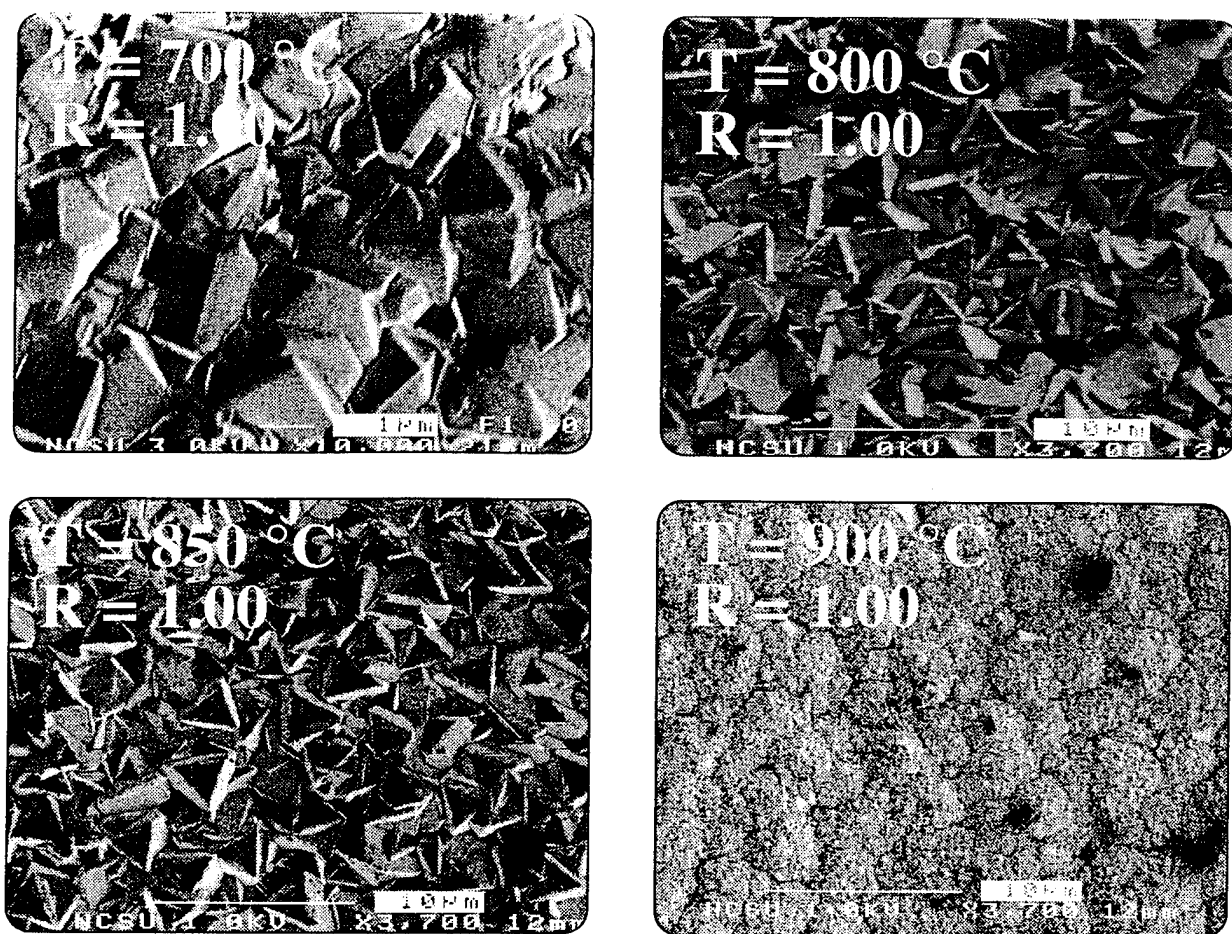


Figure 6. Effect of substrate temperature.

Mass Spectroscopy. The practical aspects of *in-situ* mass spectroscopy are demonstrated through its use in purifying our acetylene supply. The as received acetylene has a nominal purity of 99.6%, but the major impurity is acetone which is present as a solvent to reduce the flammability of acetylene. We have observed that this small amount of acetone is very detrimental to both quality and reproducibility. The acetylene is purified by passing it through a bed of activated carbon before entering the system. The purity of the acetylene was monitored after each deposition run with the QMS as shown in Fig. 10. When untreated, the ratio of acetylene ($m/e = 26$) to acetone ($m/e = 43$) is slightly less than 100. When acetylene is diverted through the activated carbon column the ratio, and thus the purity, increase by over 2 orders of magnitude. The column has a lifetime of approximately 1400 standard liters of acetylene before it requires renewal or regeneration. A fit to the data in Fig. 10 yields a breakthrough constant of 7 g carbon / liter acetylene.

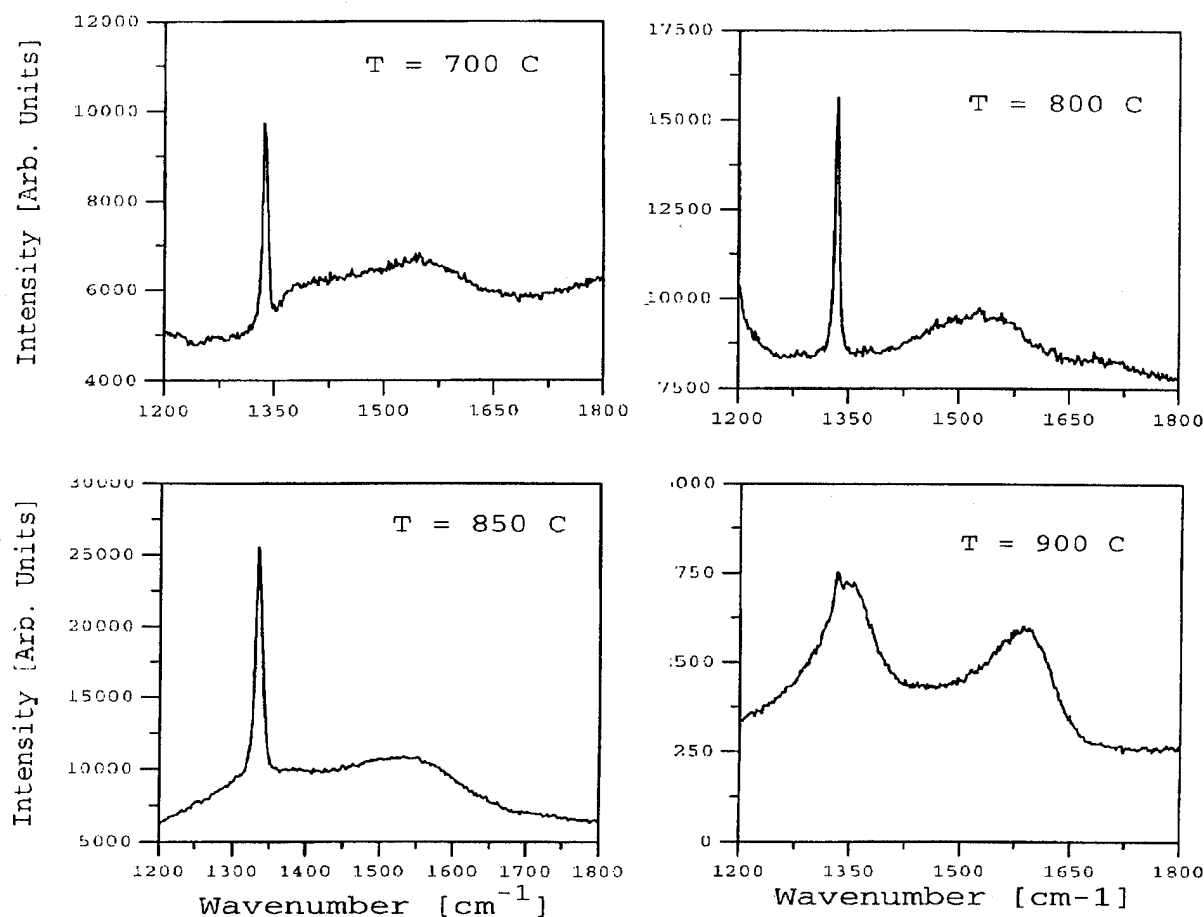


Figure 7. Temperature dependence of Raman spectrum.

Using known mixtures of acetylene and argon the sensitivity coefficient, $S_{C_2H_2,Ar}$, was determined. The data shown in Fig. 11 yields a very good fit, with a correlation coefficient better than 0.9999. Experiments are underway to determine this coefficient for the other major species individually, and also for a specialty gas mixture that has a composition characteristic of post-combustion gases.

We have also made the first *in-situ* measurements during flat flame diamond synthesis. Figs. 12 and 13 show the raw data for a number of species as a function gas composition. Although this is raw data that requires calibration before reporting absolute mole fractions, some interesting trends are observed. Over the range, $0.95 < R < 1.05$, the concentration of CO and H_2 are essentially unchanged. Over the same range hydrocarbons such as C_2H_2 and CH_4 decrease sharply while there is a concomitant increase in oxidation products like H_2O and CO_2 . Each data point represents the average of 10 individual signals which are acquired over a period of a few minutes. The error bars in Figs. 12 and 13 correspond to two standard deviations. The combination of small error bars and the strong correlation achieved in Fig. 11 will allow us to measure these species with significant accuracy.

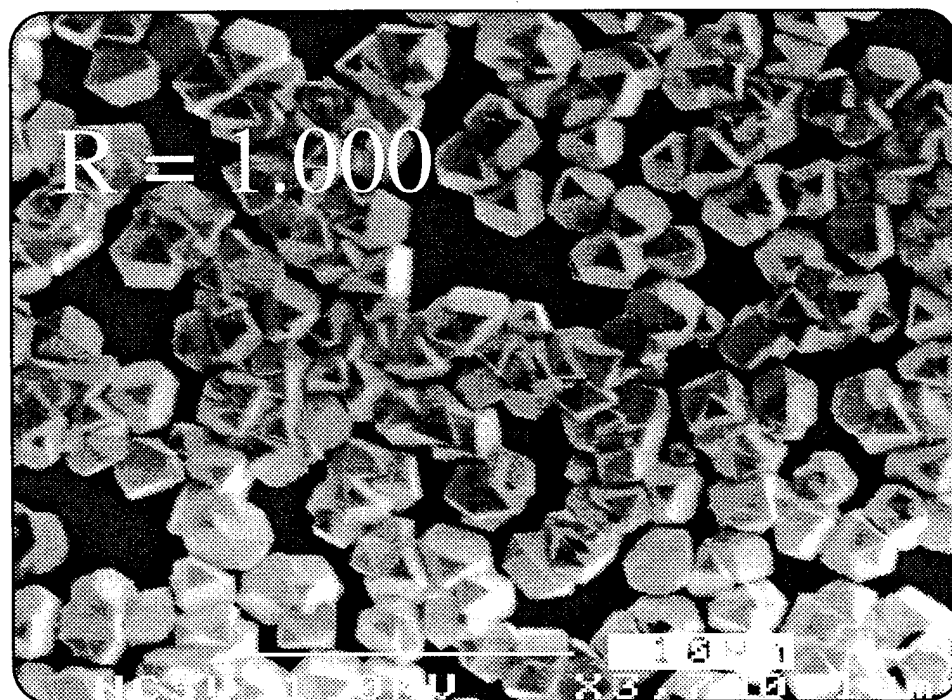
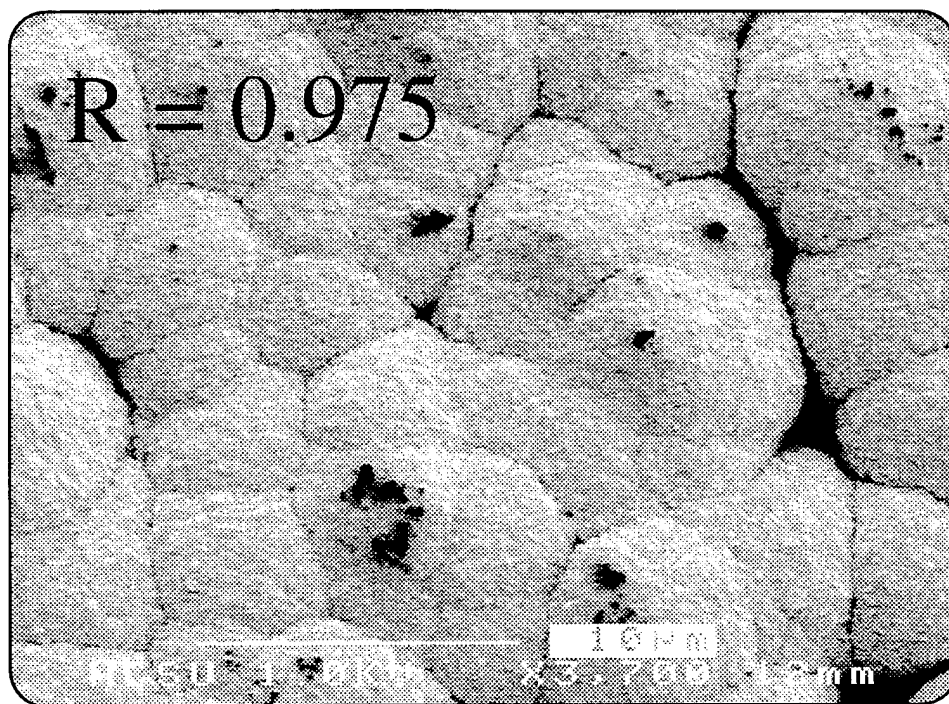


Figure 8. Dependence on gas composition.

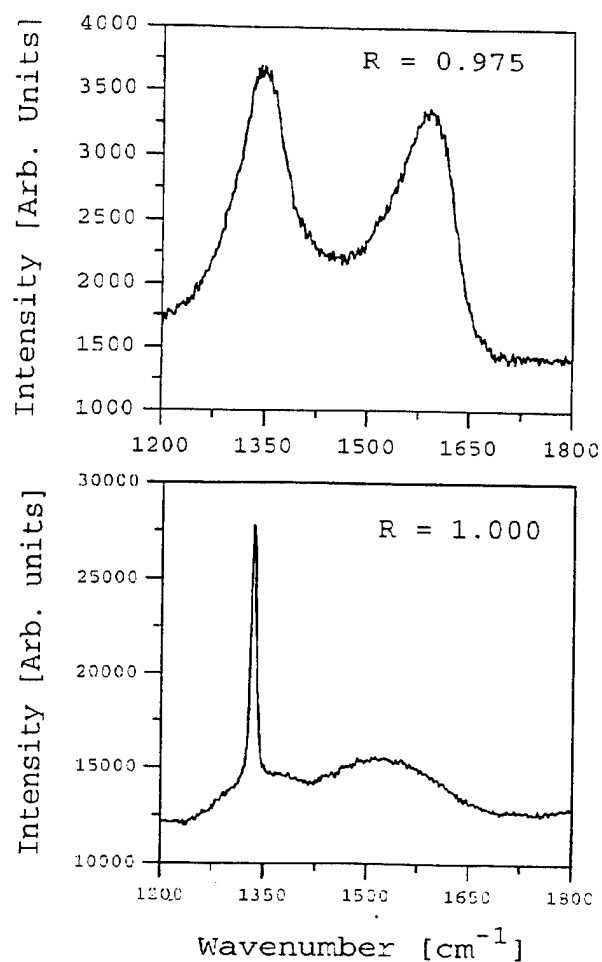


Figure 9. Composition dependence on Raman spectrum.

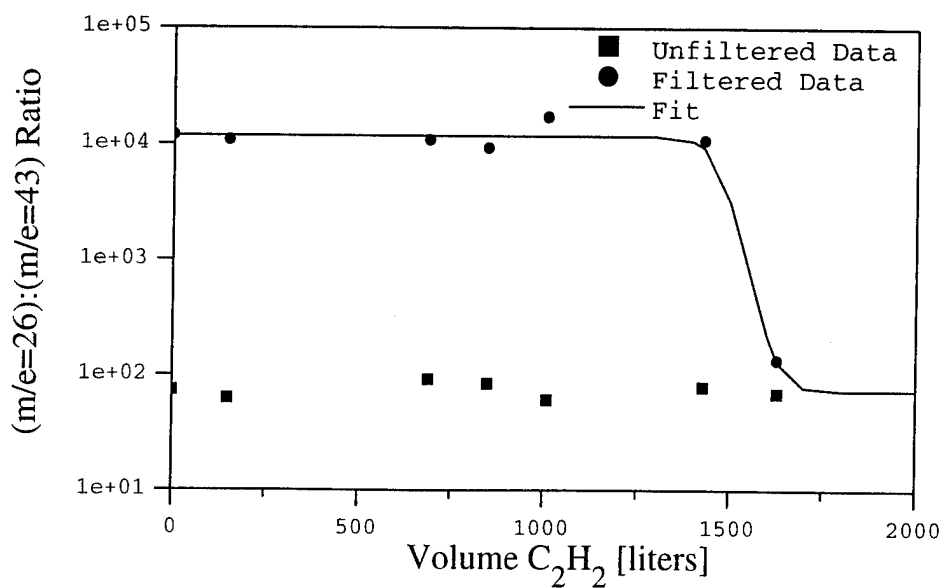


Figure 10. Loading characteristics of activated carbon filter.

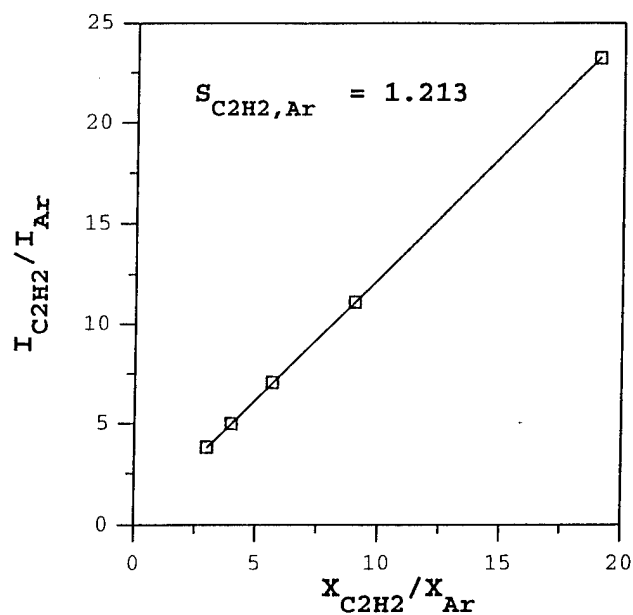


Figure 11. C_2H_2 calibration.

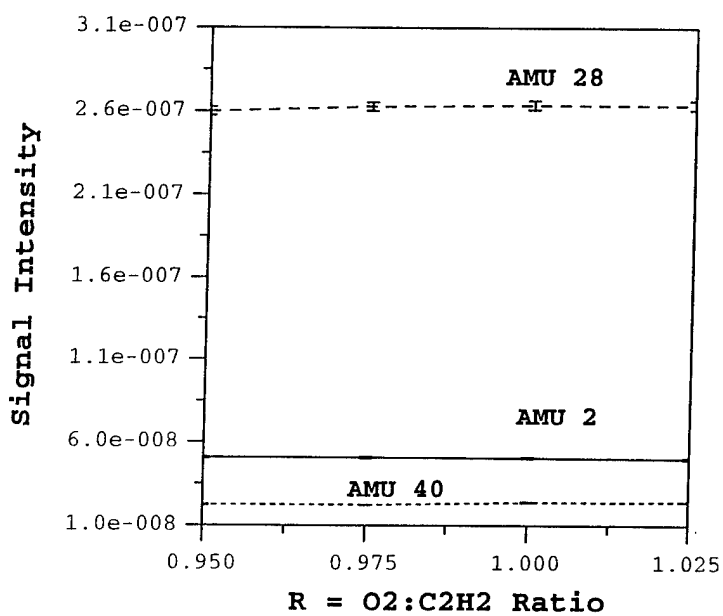


Figure 12. CO , H_2 , and Ar .

Modeling. Our first concern is understanding the strong dependence on gas composition. Equilibrium calculations provide the first insight into this question. Figure 14 plots the equilibrium mole fractions as a function of gas composition at $P = 40$ Torr. Though combustion CVD is undoubtedly a kinetic process, there is a significant relationship between the data of Fig. 12-13 and the equilibrium predictions of Fig. 14.

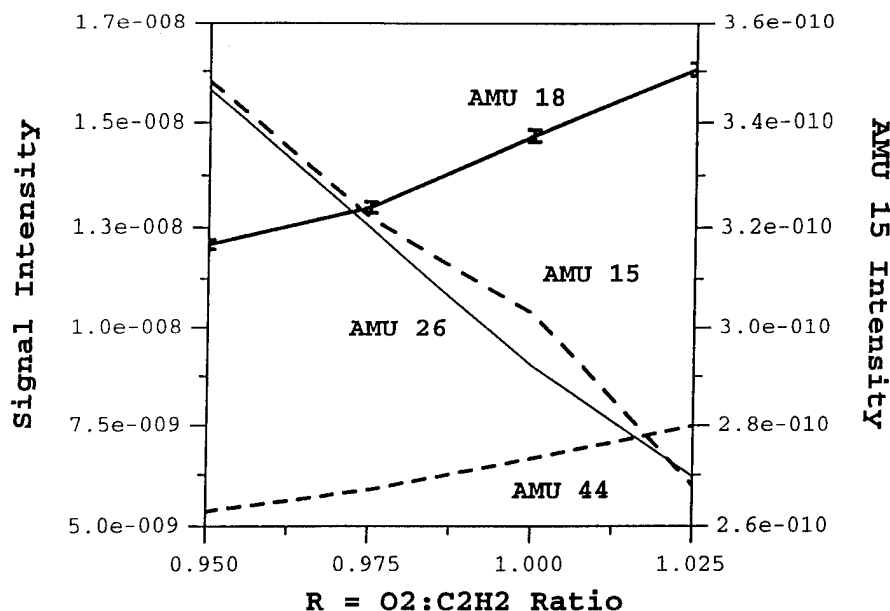
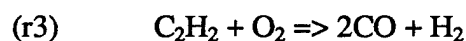


Figure 13. C_2H_2 , H_2O , CO_2 , and CH_4 .

To ensure that the CHEMKIN code was working properly, we repeated the work of Miller and Melius [8] who simulated a C_2H_2 - O_2 -Ar flame ($\phi = 2.50$, Ar = 45%). Their 51 species mechanism satisfactorily predicts the species in a 20 Torr flame that was probed using molecular beam mass spectroscopy [7]. Having established that our code was functioning properly, we modeled our typical flame: P = 40 torr, $\phi = 2.50$, Ar = 5%. The results are shown in Figs. 15-17. The overall stoichiometry of acetylene flames,



is confirmed by the major species profiles shown in Fig. 15. Fig. 16 shows the profiles of the major secondary species, atomic hydrogen and the oxidation products CO_2 and H_2O . The profile of the most commonly cited diamond precursor, CH_3 , as well as methane are shown in Fig. 17.

D. Discussion

Deposition. It useful to compare our results with other data in the literature. In general, our results are consistent with those of a previous study [5]. The biggest discrepancy is the narrow composition range that yields diamond as determined by Raman spectroscopy. In the previous study molybdenum substrates were used, and no argon was present in their flame. In addition, the flow velocity was somewhat different. We are investigating all of these aspects at present.

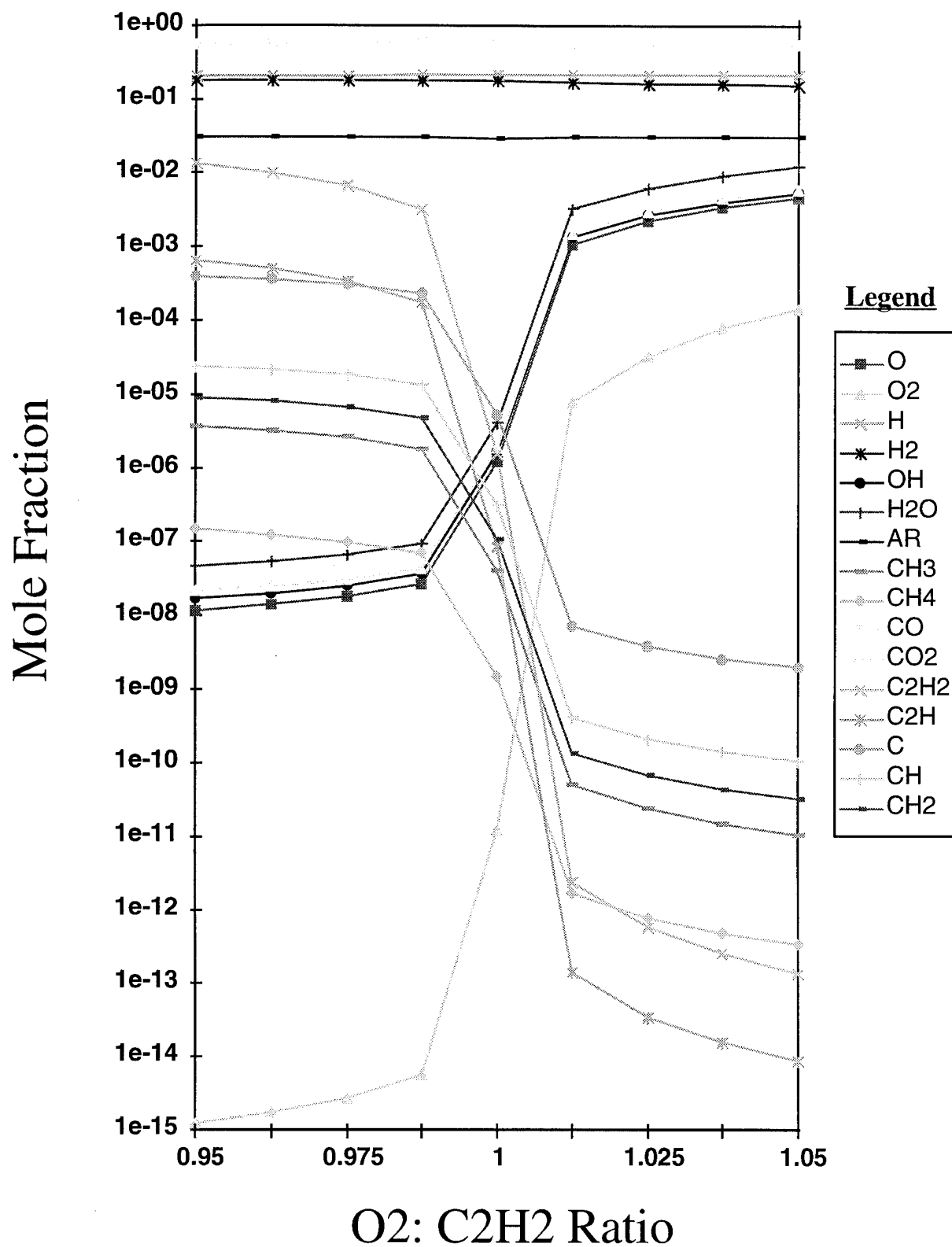


Figure 14. Equilibrium mole fractions.

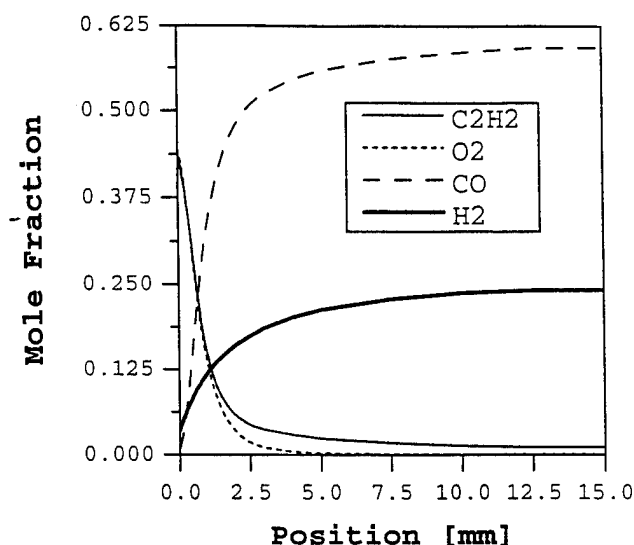


Figure 15. C_2H_2 , O_2 , CO , H_2 profiles.

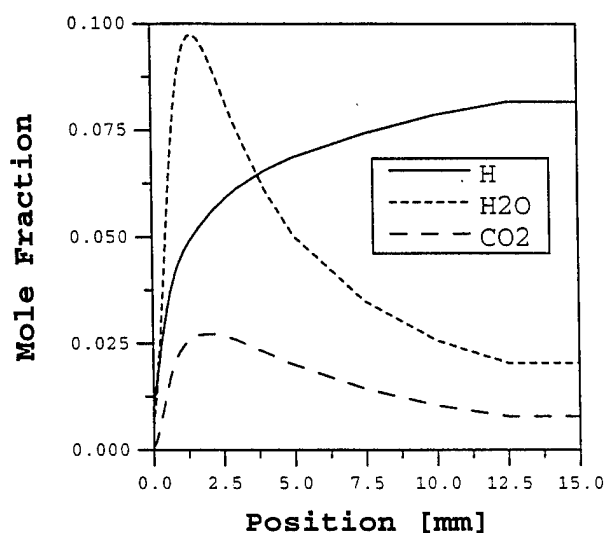


Figure 16. H_2 , H , H_2O , and CO_2 profiles.

One of our goals is to achieve $\langle 100 \rangle$ textured growth conditions. By combining this growth mode with the preferential $\langle 100 \rangle$ nucleation techniques developed at N. C. State [20, 21] we hope to grow thick films at appreciable rates which approach the quality of single crystals. We need to fully characterize the impact of burner - substrate distance, pressure, and gas-flow rate. During these studies we hope to find regimes which promote $\langle 100 \rangle$ growth.

We have also deposited thick (10-20 μm) diamond films over large areas for the fabrication of diamond sensors and membranes with collaborators at N. C. State. A cross-sectional SEM of one such film is shown in Fig. 18. Good columnar growth is observed throughout the cross-section.

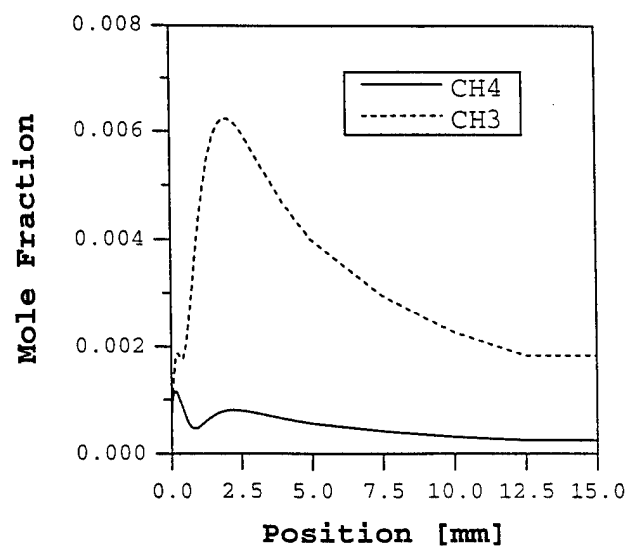


Figure 17. CH₄ and CH₃ profiles.

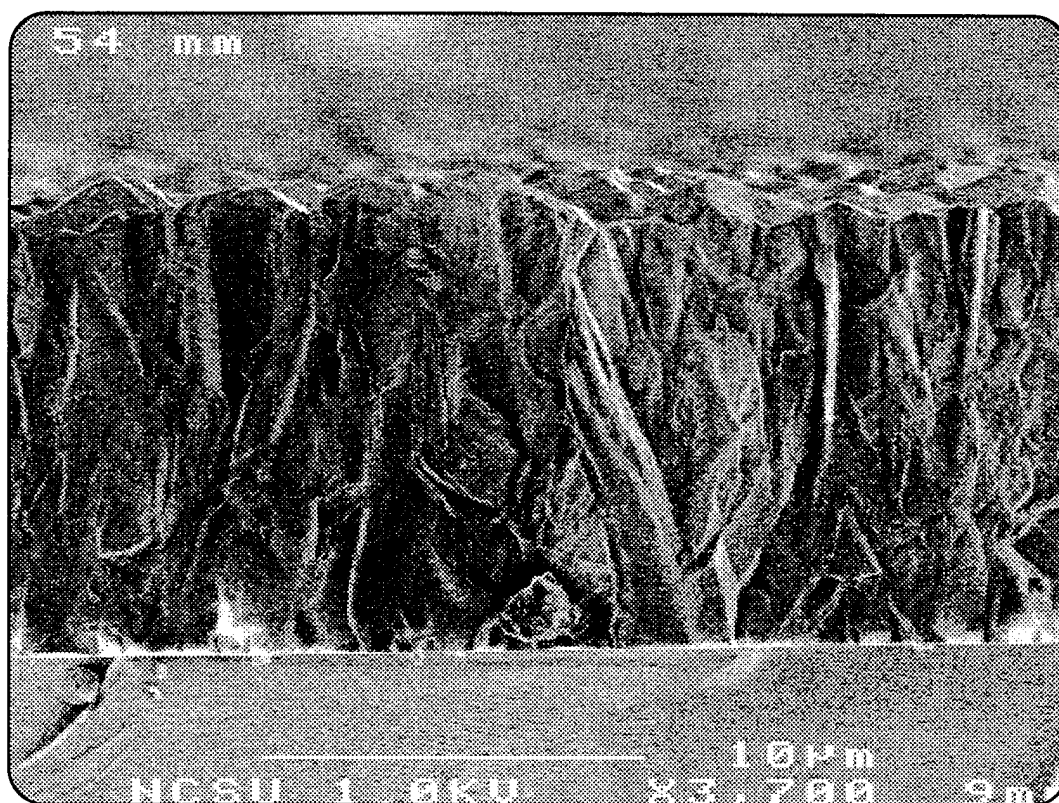


Figure 18. Cross-sectional SEM micrograph of thick film. Growth conditions: Time: 3 hrs, $T_s = 770^\circ\text{C}$, 40 Torr, $R = \text{O}_2:\text{C}_2\text{H}_2 = 1$, 5% Ar.

Mass Spectroscopy. The data in Figs. 11-13 demonstrate two points. First, the sampling techniques outlined above work satisfactorily. Second, the assumption that the species listed in Table 1 comprise the majority of the flame has been validated. Figure 19 shows the *in situ* mass spectrum of species impacting the substrate. Table II contains the peak assignments for the species outlined in Fig. 19. Additional species have a concentration less than 0.1%. In addition, it should be noted that no significant signals are detected at values of $m/e > 50$, indicating that higher hydrocarbons are not significant in our system. Interestingly, very little methane (methyl radical) is observed in the flame at conditions that yield high quality diamond at high growth rates. Further refinement of the data is required before drawing any definitive conclusions.

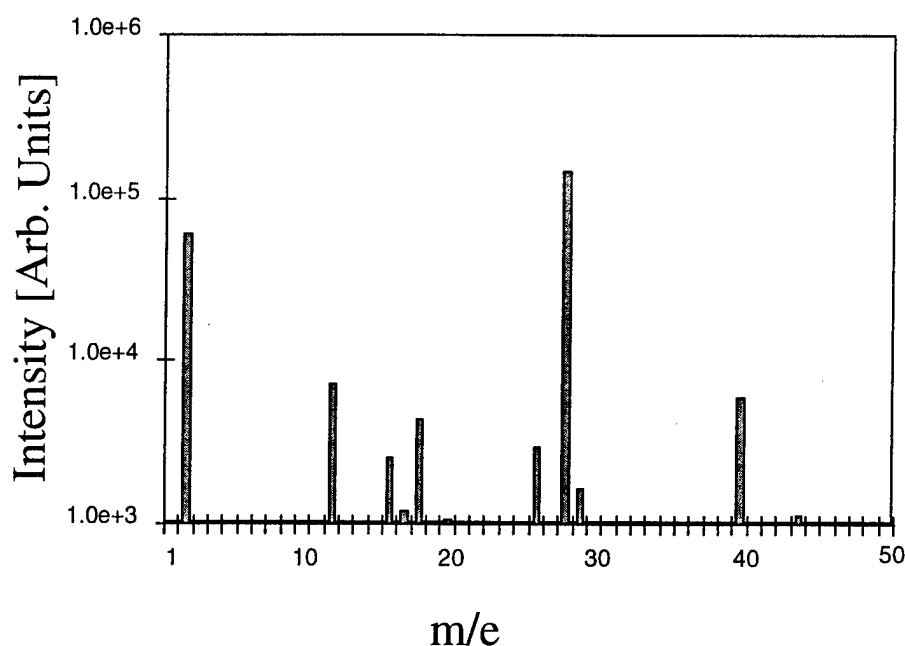


Figure 19. Mass spectrum at center of substrate. $R = 1.00$, $P = 47$ Torr, $T = 710$ C, $z = 13$ mm.

Modeling. The most interesting aspect of the flame simulations is the atomic hydrogen profile shown in Fig. 16. Typically radicals have a peaked profile, similar to methyl radical in Fig. 17. However, the atomic hydrogen concentration increases monotonically with distance from the burner. This behavior is interpreted as follows. The flame zone exists approximately 2 mm from the burner where the reactants are rapidly converted primarily into CO and H_2 as described by reaction (3) above. This mixture is near the adiabatic flame temperature, >3000 K, and cools off very slowly as it is controlled by forced convection. At this temperature more than 1/3 of a mixture of hydrogen would exist in its atomic form at equilibrium conditions. Thus, post-combustion gases approach equilibrium as they travel from

Table II. Peak Assignments for the Spectrum Presented in Fig. 19.

Channel [m/e]	Detected Species and Parent Molecule
2	H_2^+ : H_2 parent peak
12	C^+ : Fragment from CO, CO_2
16	O^+ : Fragment from CO, CO_2 , H_2O
17	OH^+ : Fragment from H_2O
18	H_2O^+ : H_2O parent peak
20	Ar^{++} : Doubly ionized argon
26	C_2H_2^+ : C_2H_2 parent peak
28	CO^+ : CO parent peak, small contribution from CO_2 fragmentation
29	C^{13}O^+ : Typical isotopic abundance, $\sim 1\%$ amu 28 peak
40	Ar^+ : Ar parent peak
$\Delta 44$	CO_2^+ : CO_2 parent peak

the burner. The final concentrations of H_2 and H at $z = 15$ mm are 24.1% and 8.2%, respectively, indicating this condition has been achieved. This may explain why such high growth rates are achieved at $z = 13$ mm. Previous workers worked at burner-substrate separations between 5 and 10 mm [4,5].

The similarity between the equilibrium predictions of Fig. 14 and the measurements of Figs. 12 and 13 indicate that the equilibrium calculation may be an efficient method to screen potential reactant compositions.

E. Conclusions

A laminar, flat combustion CVD system has been constructed. High quality deposition has been achieved over large area at high growth rates. Films have been characterized by scanning electron microscopy and Raman spectroscopy. Thick diamond samples have been deposited for applications as sensors or membranes. The effects of substrate temperature and gas ratio on deposition quality are reported. The mass sampling apparatus has been constructed and preliminary *in situ* measurements of gas phase species are described. Concurrently, simulation software has been installed for the analysis of this system. Equilibrium and premixed flame simulation have been performed.

F. Future Research Plans and Goals

The parameter investigation will be extended to characterize the impact of pressure, total flowrate, and burner-substrate separation. The effect of substrate material and argon dilution will be assessed. We will continue to characterize deposited films and identify operating regimes which promote textured film growth. Specialty gas mixtures will be used to calibrate the spectrometer, and exact mole fractions will be reported. The sampling technique will be extended to probe radical species using radical scavenging techniques. The simulations will be extended to include the stagnation-flow deposition system. Model results will be compared directly with *in-situ* measurements. Upon model validation, we will extend this work to analyze the impact of additives and alternative fuel mixtures. The combination of experimental and modeling work will be used to deduce potential growth mechanisms, and predict conditions that optimize growth.

G. References

- ⁰ Y. Hirose and N. Kondo, Program and Book of Abstracts, Japan Applied Physics 1988 Spring Meeting (Japanese Physical Society, Tokyo, 1988), p 434.
- ¹ M. Murayama, S. Kojima, and K. Uchida, J. Appl. Phys. **69**, 7924, (1991).
- ² K. F. McCarty, E. Meeks, R. J. Kee and A. E. Lutz, Appl. Phys. Lett. **63**, 1498 (1993).
- ³ N. G. Glumac and D. G. Goodwin, Mater. Lett. **18**, 119, (1993).
- ⁴ J. S. Kim and M. A. Cappelli, J. Mater. Res. **10**, 149 (1995).
- ⁵ K. V. Ravi, Diamond and Related Mater. **4**, 243 (1995).
- ⁶ E. Bastin, J-L. Delfau, M. Reullion, C. Vovelle, and J. Warnatz, *22nd Symposium (International) on Combustion*, p. 313-322, (1988).
- ⁷ J. A. Miller and C. F. Melius, Combust. Flame **91**, 21 (1992).
- ⁸ C. A. Wolden and K. K. Gleason, Appl. Phys. Lett. **62**, 2329 (1993).
- ⁹ W. L. Hsu, J. Appl. Phys. **72**, 3102, (1992).
- ¹⁰ P. W. Morrison, A. Somashekhar, J. T. Glass, and J. T. Prater, J. Appl. Phys. **78**, 4144 (1995).
- ¹¹ J. Powling, Fuel **28**, 26 (1949).
- ¹² R. M. Fristrom, Combust. Flame **50**, 239, (1983).
- ¹³ W. L. Hsu and D. M. Tung, Rev. Sci. Instrum. **23**, 4138 (1992).
- ¹⁴ R. M. Fristrom, Science **140**, 297, (1963).
- ¹⁵ R. J. Kee, F. M. Rupley, and J. A. Miller, "Chemkin II: A Fortran Chemical Kinetics Code Package for the Analysis of Gas-Phase Chemical Kinetics," Sandia National Laboratories Report, SAND89-8209, (1989).
- ¹⁶ M. E. Coltrin, R. J. Kee, G. H. Evans, E. Meeks, F. M. Rupley, and J. F. Grcar, "SPIN: A Fortran Program for Modeling One-dimensional Rotating-Disk/Stagnation-Flow Chemical Vapor Deposition Reactors", Sandia National Laboratories Report, SAND91-8003, (1991).
- ¹⁷ T. von Karman, A. Agnew. Math. Mech. **1**, 233 (1921).
- ¹⁸ E. Meeks, R. J. Kee, D. S. Dandy, and M. E. Coltrin, Combust. Flame **92**, 144 (1993).
- ¹⁹ D. S. Dandy and M. E. Coltrin, Appl. Phys. Lett. **66**, 391, (1995).
- ²⁰ P. C. Yang, W. Zhu, and J. T. Glass, J. Mater. Res. **8**, 1773 (1993).
- ²¹ B. R. Stoner, S. Sahaida, J. P. Bade, P. Southworth, and P. J. Ellis, J. Mater. Res. **8**, 1050 (1993).

III. Texture Analysis of Diamond Particles Deposited on TiC(111) by MPCVD

A. Introduction

Of the many substrates that have been used for deposition of diamond a few materials have emerged as potential heteroepitaxial substrates, namely Si [1-6], β -SiC, c-BN [7-9], Ni [10, 11], and Pt. Recently, TiC(111) [12] has been reported to be a potential heteroepitaxial substrate. Initial results revealed diamond particles were oriented to each other and pits in the substrate. To further evaluate TiC as a heteroepitaxial substrate, the substrate and the resultant diamond particles were examined for a preferential azimuthal relationship indicative of epitaxy or highly oriented deposition. The techniques employed were XRD pole figure of the substrate and diamond particles and statistical analysis of the diamond particles imaged in the scanning electron microscope (SEM).

A pole figure is a stereographic projection for a specific substrate orientation that shows the variation of pole density with pole orientation. The measured intensity is proportional to the volume fraction of crystallites having the normal to the planes bisecting the angle between the incident and diffracted beams. This technique is useful for determination of fiber and sheet texture. The experiment is conducted with the x-ray source and spectrometer at specific 2θ value for a particular substrate pole. The sample is then turned in two directions, ϕ (rotation) and ψ (tilt), about the desired pole in order to access all possible angles. As the sample is moved into position corresponding to another pole the Bragg condition will be met and a peak is recorded. If the sample consists of randomly oriented grains, the poles will be distributed uniformly over all angles. If the sample has a fiber texture, the poles will be concentrated along one tilt angle, ψ , and random along the rotation direction, ϕ . If the sample has a sheet texture, the poles will be concentrated at specific ϕ and ψ positions similar to a stereographic projection.

B. Experimental Approach

Diamond Deposition. The samples used were TiC (111) single crystal substrates from Advanced Technology and Materials, Inc. The samples were polished consecutively with 30 μ m, 6 μ m, 1 μ m, and 0.1 μ m diamond grit followed by 1 hour of polishing using 0.05 μ m Al_2O_3 to remove any residual diamond that may have been embedded in the TiC surface. After polishing, the samples were cleaned using acetone, methanol, and isopropanol. The samples were then cleaned in an H_2 plasma for 30 minutes to remove any oxide present on the surface, followed by the BEN process for 10-15 minutes. A short BEN duration, that would result in a moderate to low nucleation density, was chosen to allow observation of diamond particles separated from one another and to prevent coalescence into a complete film. This also avoided delamination of the films expected from the differences in the coefficients of thermal expansion

between diamond and TiC. The specific system parameters for each stage of the diamond deposition are listed in Table I. The deposition system used was an ASTeX 2.45 MHz 1.5kW system that has been described in detail elsewhere [13, 14].

Table I. Diamond Deposition Conditions Used on the TiC(111) in the MPCVD Chamber.

System parameter	H ₂ plasma clean	BEN	Growth
Power (W)	600	600	600
Pressure (Torr)	25	15	40
CH ₄ :H ₂ ratio	—	5%	0.2%
Bias current (mA)	—	120	—
Bias voltage (Vdc)	—	225±10	—
Temperature (°C)	660±20	785±20	900
Duration	30 min	10-15 min	8 hours

Analysis Techniques. After diamond deposition, the samples were taken to the SEM (JEOL JSM 6400F) for observation of the diamond particles. The micrographs obtained from the SEM allowed determination of the resulting diamond particle density and observation of the morphology. Also, SEM micrographs allowed the measurement of particle rotation relative to substrate features. To determine a texture preference of the diamond particles, an XRD pole figure was performed using a PHILIPS MRD X'PERT system.

C. Results and Discussion

Imaging the substrate in the SEM revealed that the diamond particle density was $1.5 \times 10^8 \text{ cm}^{-2}$ and the particles were mostly twinned. The untwinned particles had a cubo-octahedral shape that corresponds to a growth parameter, α , of slightly less than 1.5. Figure 1 shows typical diamond particles observed on the substrate. Some of the diamond particles appeared to be oriented to each other and to pyramidal pits in the substrate.

To determine if the particles had a preferred orientation, the samples were analyzed by the XRD system. At first, a 2θ scan was taken of the surface to confirm that no graphite was present within detectable limits and the diamond (111) peak was the most intense of all diamond peaks. The intensity ratios of the diamond peaks to the JCPDS file indicated the possibility of a (111) fiber texture. To confirm this fiber texture, two pole figure analyses were performed. First, a (110)_{Dia} pole figure analysis was performed. This orientation was chosen because other diamond (111) poles would appear without excessive tilting of the substrate.

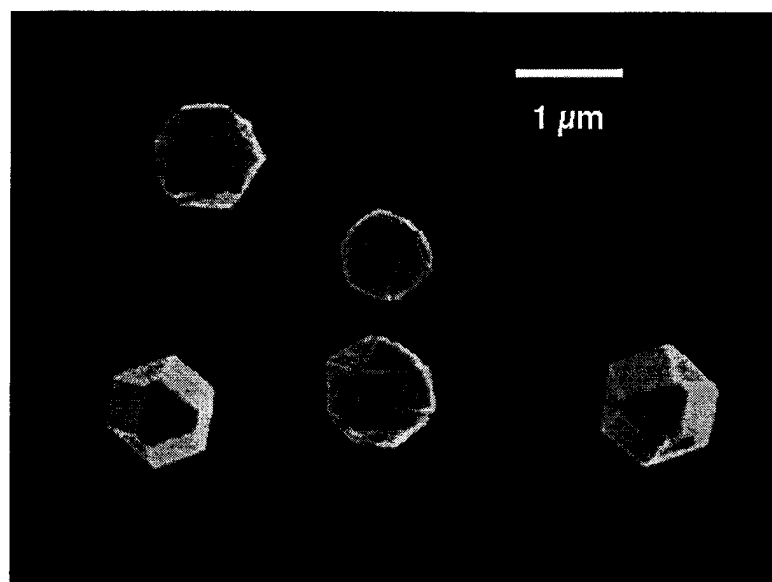


Figure 1. SEM micrograph of the diamond particles deposited on the TiC(111) substrate.

Unfortunately, the presence of the substrate $(222)_{\text{TiC}}$ plane with about the same spacing overwhelmed the signal from the diamond overlayer. However, this pole figure, slightly off axis, provided information regarding the quality of the substrate. Figure 2 shows the off-axis pole figure $(222)_{\text{TiC}}$ for the substrate. The center peak has a full width at half maximum (FWHM) value of 2° and the other poles have a FWHM value of 2.5° in both the phi and psi directions. No other features were visible above the noise level.

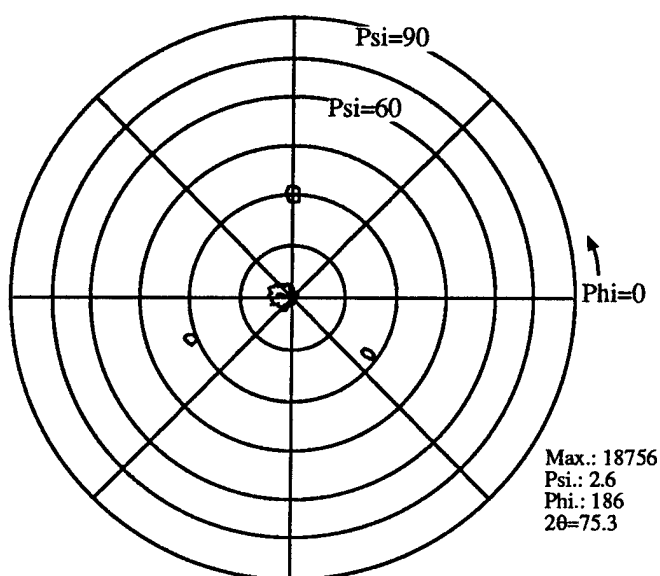


Figure 2. XRD pole figure (111) of the TiC substrate. The FWHM value of center peak was 3° and the FWHM values of the outlying peaks were 2.5° in both the phi and psi directions.

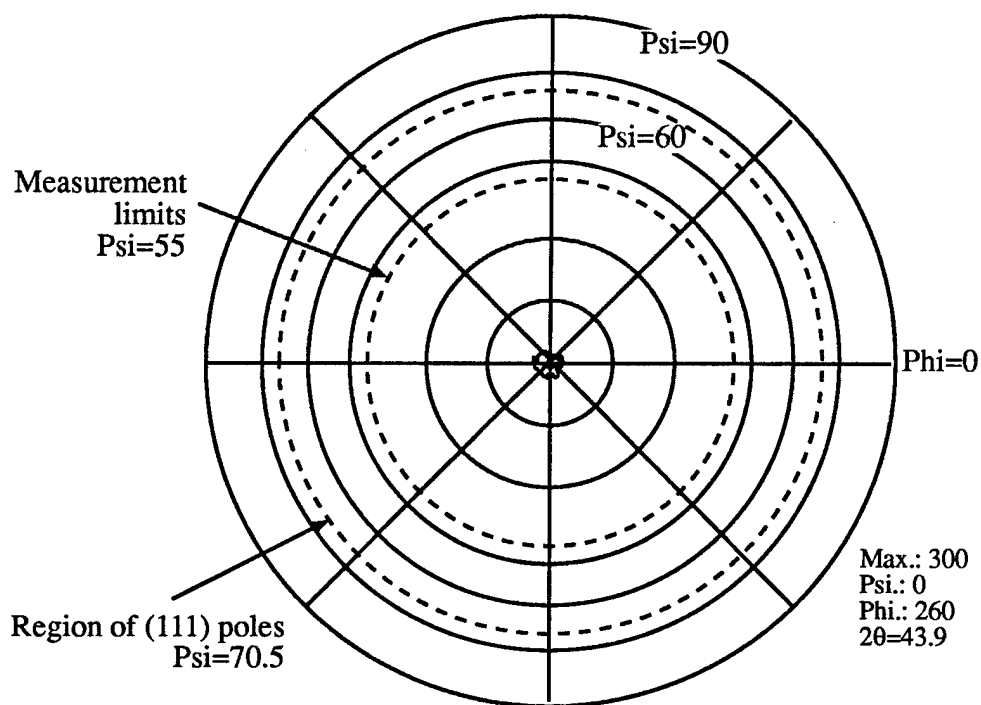


Figure 3. XRD pole figure (111) of the diamond particles. The FWHM value of the central peak was 6° indicating a fiber texture in the diamond particles.

The dominating presence of the substrate signal required using another diamond pole remoted from any substrate peaks and the diamond (111) pole was chosen for further analysis. Tilting the sample to 70.53° to observe other diamond (111) poles was not possible because the small sample size led to significant incident beam "fall off." However, the presence of the central peak (Fig. 3) indicated that the diamond particles did have a fiber texture. The FWHM of the central peak was 6° . No other features, other than the central peak, were visible above the noise level.

Because the XRD pole figure analysis could not determine an azimuthal rotation preference in the diamond overlayer, the angular distribution was determined by measuring the particles from SEM images. The micrographs were taken after the sample had been rotated such that the edge of a substrate pit was aligned with the edge of the monitor. The rotation angle of the diamond particle was the angle between a $\langle 110 \rangle_{\text{Dia}}$ direction and the bottom of the micrograph. Only those particles that were not twinned were included and the direction of rotation (clockwise(-) or counterclockwise(+)) was measured. 321 particles, approximately 25% of the imaged particles, were measured and sorted into 2° bins. The measurement error was approximately 2° . The distribution was fitted to a Gaussian distribution that had a FWHM of 3.8° . By comparing the area under the Gaussian curve to the area under the Gaussian curve's baseline, the percentage of oriented particles was calculated to be 16%, see Fig. 4.

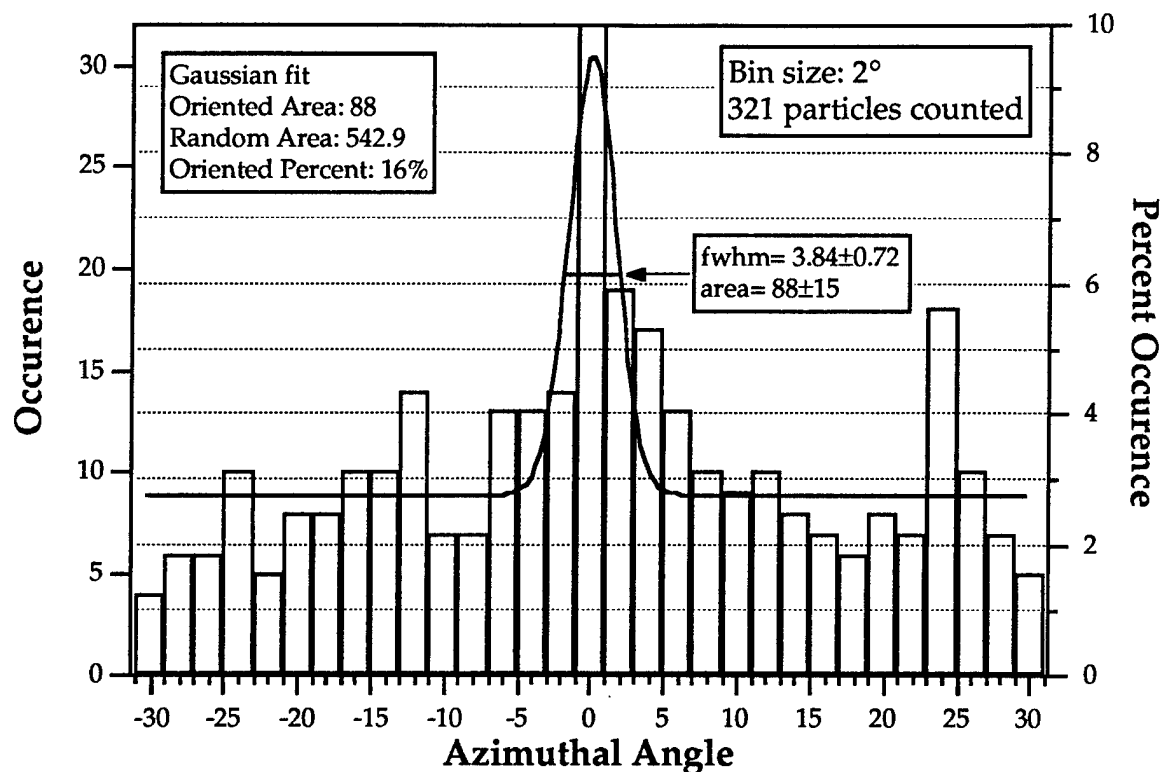


Figure 4. Histogram of azimuthal angle distribution of the diamond particles. The angles were measured from SEM micrographs and sorted into 2° bins, the approximate measurement error. The percent of oriented particles was approximately 16%.

Determination of a preferential azimuthal rotation of the diamond particles was hampered by the low number of untwinned particles. This twinning may have resulted due to several reasons. First, the growth conditions have not been optimized for suppression of twinning on the (111)_{Dia} face. Second, defects on the substrate surface may have generated defects on the diamond particles which then propagated as twins. The phase field for TiC exists over a broad range of carbon concentration (30 at.% - 50 at.%) [15]. Carbon deficiency near the surface may have disrupted the crystalline quality near the diamond nucleation site. Twinning on (111)_{Dia} face prevailed due to the low energy required for twin generation [16] and this alpha value promoted twin growth [17].

D. Conclusions

The XRD pole figure analysis of the diamond particles indicated that a (111) fiber texture was present. The sample size was too small to determine an azimuthal rotation preference from XRD pole figure analysis. Measuring the particle rotation from SEM micrographs provided a distribution of angles. Fitting the distribution to a Gaussian curve, the percentage of oriented diamond particles was determined to be 16%. The true percentage of oriented particles may have been hidden by the high density of twinned diamond particles. The source of the twins

may have been from substrate defects or gas phase conditions emphasizing twin growth. SEM micrographs revealed that the diamond particles displayed a growth parameter, α , of slightly less than 1.5.

E. Future Work

Future experiments will focus on depositing diamond under gas phase conditions that suppress twin formation and twin growth. MPCVD conditions using a low methane concentration and a high substrate temperature, α closer to 1, can reduce the amount of twinning on the (111)_{Dia} face [17]. To reduce the amount of substrate defects, thin titanium films will be carburized prior to diamond deposition. Epitaxial titanium deposition has been reported on Cu(111) and 6H-SiC(0001) substrates [18, 19]. *In vacuo* surface analysis can determine the stoichiometry of the carburized Ti layer before diamond deposition to help control the number of surface defects.

F. Acknowledgments

The authors wish to thank Advanced Technologies and Materials, Inc. for supplying the substrates and K. Gruss for her assistance with the XRD pole figure experiments. This work was funded by the Ballistic Missile Defense Organization/Innovative Science and Technology program through the Office of Naval Research.

G. References

1. D. G. Jeng, H. S. Tuan, R. F. Salat and G. J. Fricano, *Appl. Phys. Lett.* **67** (10), (1990).
2. K. Kobashi, K. Nishimura, K. Miyata, K. Kumagai and A. Nakae, *Journal of Materials Research* **5** (11), 2469-2482 (1990).
3. C. Wild, R. Kohl, N. Herres, W. Müller-Sebert and P. Koidl, *Dia. Relat. Mater.* **3**, 373 (1994).
4. B. R. Stoner, S. R. Sahaida, J. P. Bade, P. Southworth and P. J. Ellis, *Journal of Material Research* **8** (6), 1334 (1993).
5. J. Robertson, *Dia. Relat. Mater.* **4**, 549-552 (1995).
6. X. Jiang and C. L. Jia, *Appl. Phys. Lett.* **9** (28), 1197 (1995).
7. H. Meada, S. Masuda, K. Kusakabe and S. Morooka, *Dia. Relat. Mater.* **3**, 398 (1994).
8. S. Koizumi, T. Murakami, T. Inuzuka and K. Suzuki, *Applied Physical Letters* **57** (6), 563 (1990).
9. M. Kamo, H. Yurimoto and Y. Sato, "Epitaxial growth of diamond on diamond substrate by plasma assisted CVD" in *Proceedings of Proceedings of the Fourth International Conference on Solid Films and Surfaces (ICSFS-4)*, Aug 23-27 1987, Hamamatsu, Jpn., edited by p. 553-560.
10. W. Zhu, P. C. Yang and J. T. Glass, *Appl. Phys. Lett.* **63** (12), 1640-1642 (1993).
11. P. C. Yang, W. Zhu and J. T. Glass, *Journal of Materials Research* **8** (8), 1773-1776 (1993).
12. S. D. Wolter, M. T. McClure, J. T. Glass and B. R. Stoner, *Appl. Phys. Lett.* **66** (21), 2810 (1995).
13. K. L. Merkle and D. J. Smith, *Ultramicroscopy* **22**, 57-70 (1987).
14. H. Hashimoto, Y. Takai, Y. Yokota, H. Endoh and E. Fukada, *Jpn. J. Appl. Phys. Lett.* **19** (1), 1-4 (1980).

15. *Alloy Phase Diagrams*, (ASM International, Materials Park, OH, 1992), p.
16. J. C. Angus, M. Sunkara, S. R. Sahaida and J. T. Glass, *Journal of Materials Research* **7** (11), 3001-9 (1992).
17. M. A. Tamor and M. P. Everson, *Journal of Material Research* **9** (7), 1839 (1994).
18. L. M. Porter, R. F. Davis, J. S. Bow, M. J. Kim, R. W. Carpenter and R. C. Glass, *Journal of Materials Research* **10** (3), 668-679 (1995).
19. J. Vahakangas, E. D. Williams and R. L. Park, *Phys. Rev. B* **33** (4), 2281 (1986).

IV. Donor Doping of Diamond using Nuclear Transmutation

A. Introduction

Nuclear transmutation has been proposed for donor doping of diamond [1]. The goal of this process is to convert boron incorporated during growth to interstitial lithium through the reaction $^{10}\text{B}(n,\alpha)^7\text{Li}$. Calculations indicate that interstitial Li in diamond produces a shallow acceptor state [2]. This doping mechanism is of interest in diamond because of difficulties encountered in attempts to incorporate Li by more conventional means such as diffusion or incorporation during CVD. Some of the background for this work was described in the previous quarterly report.

Our approach has been to investigate transmutation in well-characterized homoepitaxial films grown by established techniques. Growth and electrical measurements have been performed at Kobe Steel USA by researchers with extensive experience in electrical measurements on homoepitaxial and polycrystalline diamond film. Our isotopically enriched boron source is diborane, one of the most common doping sources of boron for CVD diamond growth. The carrier concentration and mobility have been measured as a function of temperature prior to irradiation. In addition, our experiments include control samples with no boron and with the natural abundance of boron to separate the effects of irradiation damage from the effects of Li production. Irradiation is being performed by the Nuclear Medicine group at Oak Ridge National Laboratory which can provide a neutron flux of $2 \times 10^{15} \text{ n/cm}^2\text{s}$, yielding the desired dose in 3 days of continuous irradiation.

Table I. Samples and Target Boron Content

Sample	Boron content (Target value, cm^{-3})	Isotopic Composition
1	10^{18}	natural abundance
2	10^{20}	natural abundance
3	10^{18}	^{10}B enriched
4	10^{20}	^{10}B enriched
5	10^{20}	^{10}B enriched

All films are grown on (100) oriented type 2a natural diamond substrates. The natural isotopic abundance of boron is 19% ^{10}B and 81% ^{11}B .

B. Experimental Procedure

Homoepitaxial boron doped films have been grown using microwave CVD with diborane as the dopant source. Growth conditions were similar to previously reported work by researchers at Kobe Steel USA [3]. Table I shows the target boron concentrations for each of the five films. All films are grown on (100) oriented type 2a natural diamond substrates and range from 3 to 8 microns in thickness. The films were grown over a $3 \times 3 \text{ mm}^2$ area on the $4 \times 4 \text{ mm}^2$ substrates to isolate the films from the edges of the wafers. The edges of natural diamond wafers have a higher conductivity which has lead to anomalous results in the past. This selected area deposition also facilitates measurement of the film thickness. The isotopically enriched diborane is 96% ^{10}B and 4% ^{11}B . Films with the natural abundance of the two boron isotopes are included to aid in separating the effects of Li production from the effects of damage. The natural isotopic abundance of boron is 19% ^{10}B and 81% ^{11}B , so the maximum possible conversion of the natural abundance samples (#1 and #2) is 19%. Samples 4 and 5 have the same boron content to provide a duplicate experiment. In addition, measurements can be made of the back surfaces of the diamond wafers to analyze the effects of neutron irradiation on diamond which is free of boron.

Metal contacts consisting of Ti and Au were applied. The carrier concentration and mobility were measured at several temperatures from 300 to 600 K using the Hall effect in a van der Pauw geometry. Descriptions of the metallization process and Hall measurements can be found in publications by researchers at Kobe Steel [3].

Raman and photoluminescence spectroscopy were used to provide a baseline measurement of the quality and defects in the films and substrates. It is expected that the films will be damaged during the irradiation process, so it is important to measure the quality of the films before irradiation. Raman measurements were made using the 5145\AA line of an Argon laser, and photoluminescence measurements using the 4579\AA line (2.71 eV). The incident light was focused to a $10\text{ }\mu\text{m}$ spot size using a microscope, and the scattered light was analyzed using an ISA U-1000 scanning double monochromator.

Samples were irradiated by Dr. Saed Mirzadeh of the Nuclear Medicine Group at Oak Ridge National Laboratory. The irradiation flux was $2 \times 10^{15} \text{ n/cm}^2$ and the total dose was $3 \times 10^{20} \text{ n/cm}^2$.

C. Results and Discussion

Raman and PL spectra were similar for all of the samples. Raman spectra showed only the 1332 cm^{-1} diamond peak, as would be expected for homoepitaxial films. A typical Raman spectrum is shown in Fig. 1. The line to the left of the 1332 cm^{-1} peak is an emission line from the argon plasma. The PL spectra showed a broad band luminescence peaked at 2.4 eV with a line width about 0.3 eV. This band has been observed previously in both synthetic and natural

diamond and is referred to as band A luminescence. It is associated with the presence of nitrogen in the diamond. PL spectra were similar when measured from the back side of the substrate, indicating that the nitrogen is in the substrate rather than just the film.

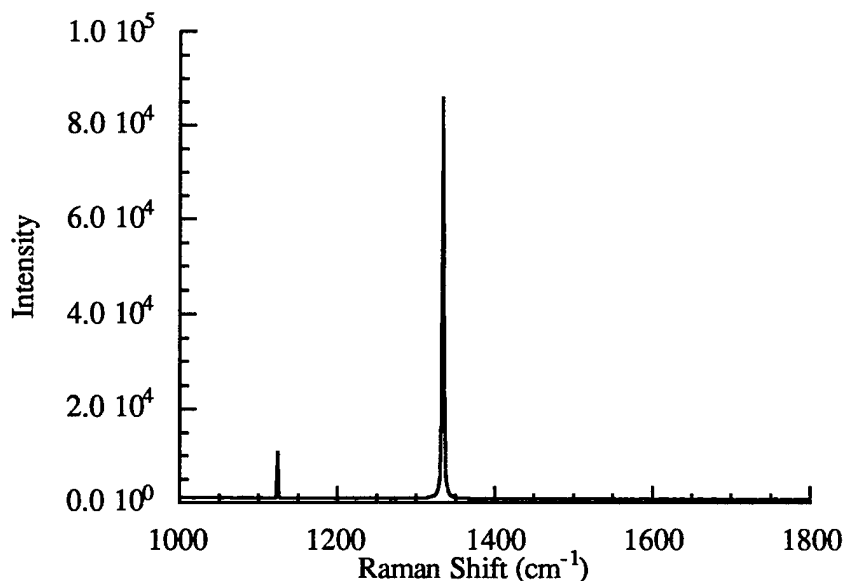


Figure 1. Typical Raman Spectrum of sample before irradiation.

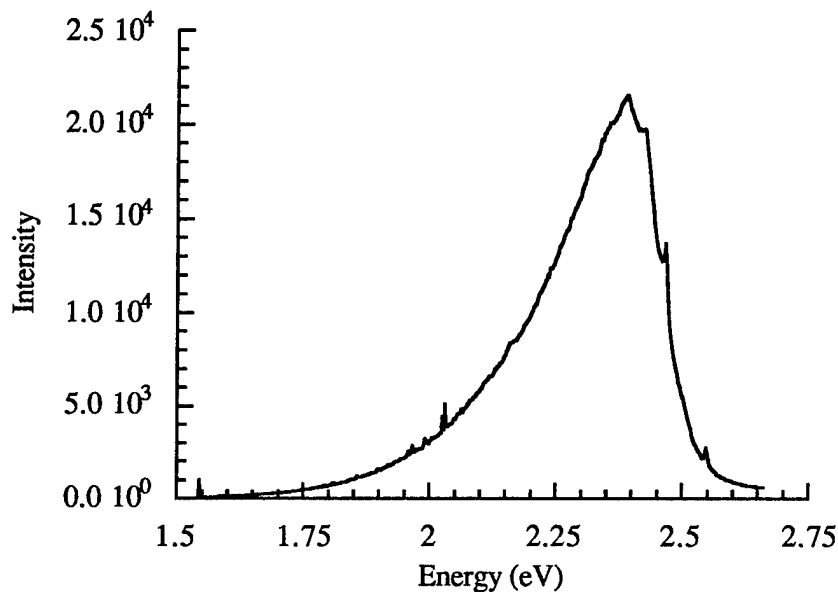


Figure 2. Typical Photoluminescence Spectrum of sample before irradiation. Excitation energy is 2.71 eV.

The diamond samples were irradiated at a dose of 3×10^{20} n/cm². The samples exhibited a greater radioactivity than expected when removed from the reactor. As of 2/26/96, the package

read 1 R/h unshielded and ~64 mR/h shielded with 1" lead. Gamma ray spectroscopy performed by Dr. Mirzadeh indicated 1-3mCi of ^{46}Sc as the major activity. The half life of ^{46}Sc is 83 days, so the decay time to $<1\mu\text{Ci}$ would be 19-22 months. The scandium is probably in the natural diamond samples because ^{46}Sc is typically not observed in the packaging materials. However, the diamond samples have not yet been removed from all of the packaging materials. Testing the diamond separately from the packaging will be one of the next steps to determine whether it will be necessary to work with radioactive samples.

D. Conclusions

In summary, nuclear transmutation is being investigated as a means for donor doping of diamond. To date samples have been prepared for irradiation, baseline electrical measurements and optical measurements have been performed, and samples have been irradiated at a dose of $3 \times 10^{20} \text{ n/cm}^2$.

E. Future Research Plans and Goals

The next steps in the project are (1) confirmation that the diamond samples are the source of the radioactivity, and (2) characterization and annealing studies post irradiation. The post irradiation studies will be more involved than expected if the diamond substrates are in fact the source of the radioactivity. It is possible that the activity is in the packaging material. The extent of the post irradiation studies will also be determined by the amount of damage produced in the irradiation process. The diamond samples will be removed from the packaging and tested separately from the aluminum spacers. Samples will also be visually inspected for damage induced by the irradiation.

Post irradiation studies will begin with optical assessment of the damage via Raman and photoluminescence spectroscopy. For the Raman, the radioactive samples could be shielded except for an opening for the beam. For the annealing, radioactive samples would probably need to be sealed in a quartz tube so that no radioactive material could be left in the furnace. Electrical characterization will be pursued if the radiation damage can be recovered.

F. References

1. B. Spitsyn, G. Popovici & M. A. Prelas, Second International Conference on the Applications of Diamond Films and Related Materials, edited by M. Yoshikawa, M. Murakawa, Y. Tzeng & W. A. Yarbrough (Tokyo, Japan, 1993) 57-64.
2. S. A. Kajihara, A. Antonelli, J. Bernholc & R. Car, Physical Review Letters **66**, 2010 (1991).
3. D. M. Malta, J. A. V. Windheim, H. A. Wynands & B. A. Fox, Journal of Applied Physics **77**, 1536-1545 (1995).

V. Distribution List

Mr. Max Yoder Office of Naval Research Electronics Division, Code: 312 Ballston Tower One 800 N. Quincy Street Arlington, VA 22217-5660	3
Administrative Contracting Officer Office of Naval Research Regional Office Atlanta 101 Marietta Tower, Suite 2805 101 Marietta Street Atlanta, GA 30323-0008	1
Director, Naval Research Laboratory ATTN: Code 2627 Washington, DC 20375	1
Defense Technical Information Center Bldg. 5, Cameron Station Alexandria, VA 22314	2